aerospace

MDPI

Article

Semi-Closed-Form Solution of Near-Minimum-Time Spin-to-Spin Attitude Maneuvers

Seong-Hyeon Jo and Sung-Hoon Mok *

Department of Aerospace Engineering and Program in Aerospace Systems Convergence, Inha University, Incheon 21999, Republic of Korea; shjo@inha.edu

* Correspondence: shmok@inha.ac.kr; Tel.:+82-32-350-9022

Abstract

High-agility spacecraft require time-efficient attitude maneuvers under strict actuator- and system-driven saturation limits on angular rate and angular acceleration. Analytical methods for attitude profile generation are attractive for on-board use because of their deterministic structure and low computational burden; however, depending on boundary conditions and sequential constraint-enforcement logic, they may yield either infeasible commands that violate constraints or overly conservative commands that underutilize available authority and unnecessarily prolong maneuver time. In contrast, numerical optimization-based methods can produce (near-)minimum-time solutions but are often too iterative and tuning-sensitive for real-time deployment. The proposed method produces an iteratively refined closed-form solution. The inner loop yields a closed-form solution for a given set of parameters, while the outer loop updates the parameter set via an iterative rescale step. The resulting finite-jerk (jerk-limited) profiles are intended for use in a feedforward–feedback architecture to mitigate terminal mismatch induced by quaternion-kinematics linearization and acceleration-related variable mappings. Numerical studies evaluate the proposed method using representative single-case examples and Monte Carlo simulations with comparisons against a baseline analytical method and a numerical optimization-based method. These results indicate that the proposed approach substantially improves feasibility and optimality such that it achieves maneuver times close to those of numerically optimized solutions, while maintaining a semi-closed-form structure.

Keywords: agile spacecraft; attitude profile generation; semi-closed-form solution; finite-jerk commands; constraint enforcement

Check for updates

Academic Editor: Dario Modenini

Received: 27 January 2026
Revised: 20 February 2026
Accepted: 26 February 2026
Published: 4 March 2026

Copyright: © 2026 by the authors. Licensee MDPI, Basel, Switzerland. This article is an open access article distributed under the terms and conditions of the Creative Commons Attribution (CC BY) license.

1. Introduction

High-agility spacecraft missions—including Earth observation, space situational awareness, formation flying, and space-based surveillance—increasingly demand large-angle attitude reorientations within short time windows. Such maneuvers need to be time-efficient while strictly complying with actuator-driven path constraints, most notably limits on angular rate and angular acceleration. Accordingly, generating feasible and near-time-optimal attitude command profiles has been extensively studied and remains a central topic in spacecraft attitude control.

Broadly, two methodological approaches have been adopted for attitude command generation: *analytical methods* and *numerical optimization-based methods*. Analytical methods have been developed to produce closed-form (or semi-closed-form) command profiles that can be evaluated with minimal computational burden, which is attractive for on-board

use under resource-limited flight processors. Representative studies include closed-form solutions derived by classifying feasible maneuver-profile structures under prescribed constraints [1], smooth single-eigenaxis-based minimum-jerk slew profiles [2], designs that combine minimum-time segments with stabilization periods [3], and closed-form solutions for minimum-effort maneuvers formulated as two-point boundary-value problems using eigenaxis parameterizations [4]. Despite their deterministic structure and efficiency, these approaches often rely on eigenaxis-aligned boundary conditions; consequently, they are not readily generalizable to arbitrary maneuver scenarios in which the boundary conditions cannot be consistently represented with respect to a single eigenaxis. Moreover, eigenaxis maneuvers are not always minimum-time solutions under realistic constraints [5,6]. To address general spin-to-spin maneuver problems with arbitrary boundary conditions that cannot be consistently defined with respect to a single eigenaxis, a segmented analytical method has been proposed, wherein the maneuver is decomposed into multiple phases (e.g., spin-to-rest, rest-to-rest, and rest-to-spin segments) so that each segment can be treated analytically [7]. However, multi-phase decompositions can increase maneuver time due to intermediate switching and stabilization requirements; to mitigate this challenge, a single-phase small-angle closed-form solution was introduced in [8]. Overall, while closed-form solutions are attractive for rapid planning and on-board implementation, their ability to achieve time-optimal performance is inherently limited, and their applicability may be restricted by simplifying assumptions; moreover, the coupling among profile parameters imposed by the boundary conditions can inherently lead to accumulated conservatism.

In contrast, numerical optimization-based methods can directly handle nonlinear dynamics and constraints, which can yield solutions closer to a minimum-time solution. In particular, pseudospectral (PS) methods have been extensively applied to minimum-time attitude maneuvers for spacecraft equipped with diverse actuators such as magnetic torquers, reaction wheels, and control moment gyros (CMGs) [9–12]. Flight-oriented demonstrations have further shown that PS-based solutions can be computed, validated, and uplinked to flight software for successful execution [13]. Alternative numerical approaches based on inverse dynamics have also been investigated for minimum-time reorientation [14,15]. Nevertheless, numerical solvers typically involve iterative optimization, case-specific parameter tuning, and reasonably informed initial guesses; they may require appreciable computational effort and their performance can depend on problem conditioning, which complicates their deployment for real-time or on-board use. On the other hand, a practical limitation observed in baseline analytical methods is that, under bounded rate and acceleration constraints, they might produce either *infeasible* profiles that violate constraints or *overly conservative* profiles that satisfy constraints but underutilize available control authority, resulting in unnecessarily long maneuver times [8]. Motivated by the complementary strengths and limitations of analytical and numerical methods, this paper proposes a *semi-closed-form solution* that augments a closed-form solution for a given set of parameters with an iterative rescale step. The proposed method preserves the analytical profile structure and boundary-condition consistency while iteratively adjusting maneuver parameters to (i) recover feasibility when the baseline analytical profile violates constraints and (ii) mitigate conservatism by improving optimality when the baseline solution is overly conservative.

The main contributions of this work are summarized as follows: (i) We identify and characterize the *infeasible* and *overly conservative* phenomena that arise in analytical command generation under bounded angular-rate and angular-acceleration constraints. (ii) We develop a semi-closed-form solution that restores feasibility and improves optimality while preserving the analytical profile structure and boundary-condition consistency. (iii) We demonstrate the control-oriented validity of the proposed approach by showing that resid-

ual terminal mismatch can be practically compensated through feedforward–feedback tracking, thereby supporting the closed-loop applicability of the proposed semi-closed-form command generator.

The remainder of this paper is organized as follows. Section 2 formulates the spin-to-spin maneuver problem and the associated constraints. Section 3 presents the process of the semi-closed-form solution and the iterative rescaling logic. Section 4 provides numerical results, including comparative evaluations against baseline analytical method and numerical optimization-based method, and illustrates how feedback tracking alleviates terminal mismatch in practice. Finally, Section 5 concludes the paper by summarizing the main findings and discussing practical implications.

2. Problem Definition

This section formulates the minimum-time spin-to-spin attitude maneuver problem. The boundary conditions at the initial and final times, t_0 and t_f, are prescribed as

$$\mathbf{q}(t_0) = \mathbf{q}_0, \qquad \boldsymbol{\omega}(t_0) = \boldsymbol{\omega}_0, \tag{1}$$

$$\mathbf{q}(t_f) = \mathbf{q}_f, \qquad \boldsymbol{\omega}(t_f) = \boldsymbol{\omega}_f. \tag{2}$$

where $\mathbf{q} = [\, q_1 \; q_2 \; q_3 \; q_4 \,]^T = [\, \mathbf{q}_v^T \; q_4 \,]^T \in \mathbb{R}^4$ denotes the unit quaternion satisfying $\|\mathbf{q}(t)\| = 1$, and $\boldsymbol{\omega} = [\, \omega_1 \; \omega_2 \; \omega_3 \,]^T \in \mathbb{R}^3$ denotes the body angular velocity. The final time t_f is free to be minimized.

Along the maneuver, the spacecraft is subject to actuator-driven path constraints. This paper considers two sets of constraints. The first set represents the hardware performance limits on angular rate and angular acceleration:

$$|\omega_i(t)| \le \omega_{\max,i}, \qquad i = 1, 2, 3, \tag{3}$$

$$|\alpha_i(t)| \le \alpha_{\max,i}, \qquad i = 1, 2, 3, \tag{4}$$

where $\boldsymbol{\omega}_{\max} = [\, \omega_{\max,1} \; \omega_{\max,2} \; \omega_{\max,3} \,]^T$ and $\boldsymbol{\alpha}_{\max} = [\, \alpha_{\max,1} \; \alpha_{\max,2} \; \alpha_{\max,3} \,]^T$ define box-shaped admissible sets for $\boldsymbol{\omega}(t)$ and $\boldsymbol{\alpha}(t)$, respectively; each element is the saturation limit for the corresponding body axis. Axis-wise angular-rate and angular-acceleration bounds such as (3)–(4) are widely used in time-/effort-optimal attitude maneuver formulations to represent spacecraft-level actuator limits, allowing axis-dependent saturation levels via $\omega_{\max,i}$ and $\alpha_{\max,i}$ [5,6,16].

To suppress micro-vibrations induced by discontinuous changes in the commanded angular acceleration, we employ a finite-jerk command structure. The jerk input is defined as the time derivative of angular acceleration, $\boldsymbol{j}(t) \triangleq \dot{\boldsymbol{\alpha}}(t)$. As illustrated in Figure 1, the finite- and infinite-jerk profiles are distinguished by the transition time t_r, i.e., the duration required for $\boldsymbol{\alpha}(t)$ to reach its peak magnitude: $t_r > 0$ produces a finite-jerk (continuous-acceleration) command, whereas $t_r = 0$ corresponds to an infinite-jerk profile with discontinuous acceleration. Accordingly, selecting a nonzero t_r imposes the bounded-jerk condition

$$-\frac{\boldsymbol{\alpha}_{\max}}{t_r} \le \boldsymbol{j}(t) \le \frac{\boldsymbol{\alpha}_{\max}}{t_r}, \tag{5}$$

where $\boldsymbol{j}(t) \in \mathbb{R}^3$ is the jerk input.

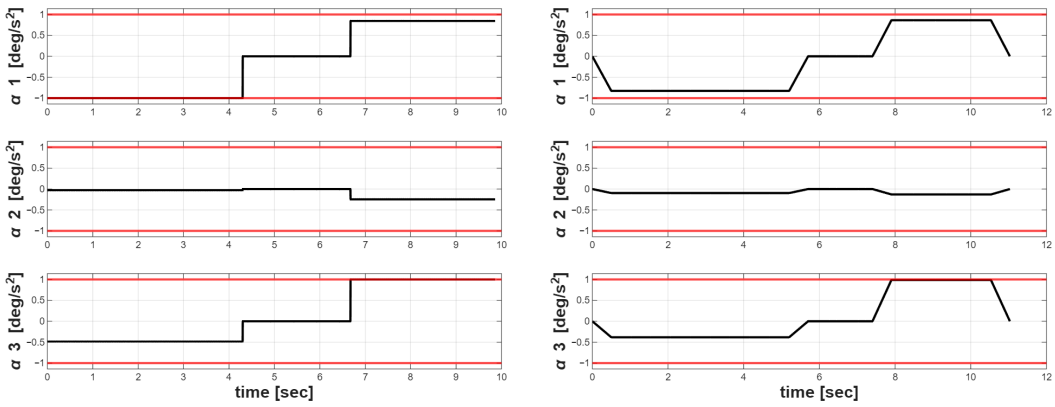


Figure 1. Input command profiles. (**a**) Infinite-jerk input ($t_r = 0$). (**b**) Finite-jerk input ($t_r > 0$).

The second set of path constraints is given by the third-order attitude kinematics. In this kinematics-level formulation, torque/inertia dynamics are not modeled explicitly; instead, angular acceleration and jerk are introduced to capture the finite-jerk behavior:

$$\dot{\mathbf{q}}(t) = \frac{1}{2}\,\Xi(\mathbf{q}(t))\,\boldsymbol{\omega}(t), \tag{6}$$

$$\dot{\boldsymbol{\omega}}(t) = \boldsymbol{\alpha}(t), \tag{7}$$

$$\dot{\boldsymbol{\alpha}}(t) = \boldsymbol{j}(t), \tag{8}$$

with

$$\Xi(\mathbf{q}) = \begin{bmatrix} q_4 & -q_3 & q_2 \\ q_3 & q_4 & -q_1 \\ -q_2 & q_1 & q_4 \\ -q_1 & -q_2 & -q_3 \end{bmatrix}. \tag{9}$$

Actuation Assumption

The bounds in (3)–(5) are used as an axis-wise abstraction of the available attitude control authority and correspond to the commonly adopted fully-actuated formulation in time-/effort-optimal attitude maneuvers. Specifically, three independent body-axis control channels are assumed to be available within prescribed limits, which supports an analytic (semi-closed-form) treatment at the kinematics level. In practice, actuator geometry and internal constraints (e.g., reaction-wheel momentum saturation, CMG singularities, or thruster allocation limits) can yield a non-axis-aligned attainable set and may lead to effectively underactuated cases (e.g., two-axis control authority), for which an explicit actuator model and a control allocation layer are required. The present formulation, however, already accommodates anisotropic capabilities through axis-dependent limits $\omega_{\max,i}$ and $\alpha_{\max,i}$, which are directly handled by the proposed procedure.

3. Semi-Closed-Form Solution

3.1. Procedure for Attitude Profile Generation

Figure 2 summarizes the procedure used to construct the proposed semi-closed-form attitude maneuver profile. In the conventional analytical framework, path constraints are enforced by sequential downscaling. Although each step satisfies the currently active bound, repeated application can accumulate conservatism—often appearing as an *overly conservative* profile with degraded optimality—and may occasionally yield an *infeasible* solution after subsequent updates due to parameter coupling. To mitigate these effects,

the proposed method augments the baseline procedure with an additional *rescale* refinement loop (highlighted in orange in Figure 2) that compensates for accumulated downscaling while preserving feasibility.

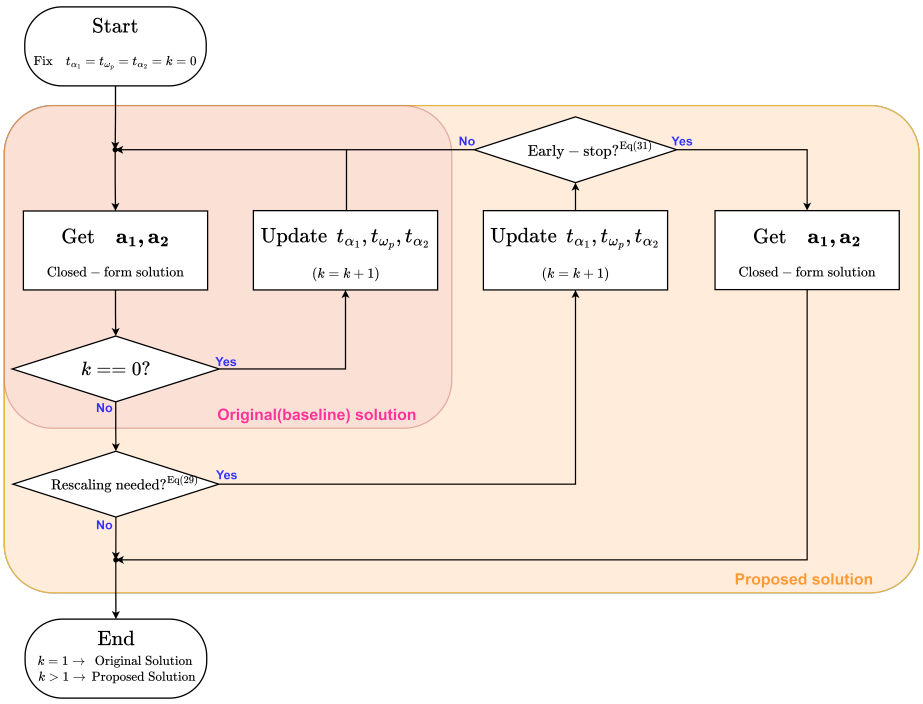
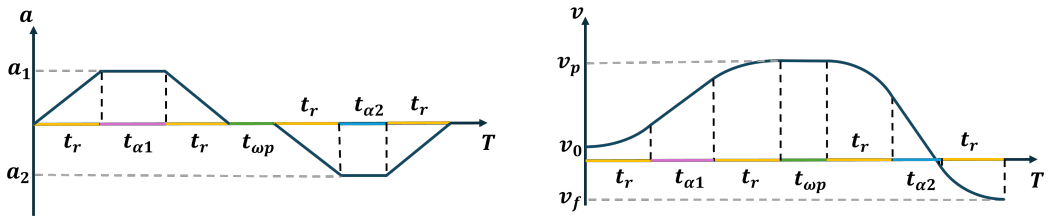


Figure 2. Flow chart for obtaining the proposed semi-closed-form solution. *Notation:* t_{α_1}, t_{ω_p}, and t_{α_2} denote the phase durations during which the first angular-acceleration constraint, the angular-rate constraint, and the second angular-acceleration constraint are active (i.e., saturated), respectively; $\mathbf{a}_1$ and $\mathbf{a}_2$ represent the corresponding constant quaternion-acceleration vectors. The *Update* $(t_{\alpha_1}, t_{\omega_p}, t_{\alpha_2})$ and *Get* $(\mathbf{a}_1, \mathbf{a}_2)$ blocks perform variable-update computations, as described in Section 3.4.

3.1.1. Baseline (Original) Solution

The baseline solution follows the original analytic procedure developed in Ref. [8]; for completeness, this subsection briefly summarizes the steps used to obtain the baseline profile. The procedure starts by initializing the phase durations to zero, $t_{\alpha_1} = t_{\omega_p} = t_{\alpha_2} = 0$, and setting the iteration index to $k = 0$ (Start block in Figure 2). As illustrated in Figure 3, t_{α_1}, t_{ω_p}, and t_{α_2} denote the phase durations during which the first angular-acceleration constraint, the angular-rate constraint, and the second angular-acceleration constraint are active (i.e., saturated), respectively. Given the boundary conditions, the closed-form relations first provide the unconstrained profile parameters in terms of $(\mathbf{a}_1, \mathbf{a}_2)$ (Get $\mathbf{a}_1, \mathbf{a}_2$ block). Here, $\mathbf{a}_1$ and $\mathbf{a}_2$ represent the constant quaternion-acceleration levels, i.e., the second time derivative of the quaternion implied by the linearized kinematics in Equations (10) and (11). Their definition and usage are summarized in Section 3.2. When $k = 0$ (decision block $k = 0$), the phase durations $(t_{\alpha_1}, t_{\omega_p}, t_{\alpha_2})$ are updated through a single pass of the sequential scaling rule, and the counter is incremented ($k \leftarrow k + 1$) (Update $t_{\alpha_1}, t_{\omega_p}, t_{\alpha_2}$ block in the pink region). Using these updated durations, the algorithm returns to the closed-form computation to re-evaluate $(\mathbf{a}_1, \mathbf{a}_2)$, yielding the baseline solution (i.e., the $k = 1$ output of the original procedure).



(**a**) (**b**)

Figure 3. Parameterized maneuver profiles in the linearized domain. (**a**) Quaternion-acceleration profile $\mathbf{a}(t)$. (**b**) Quaternion-velocity profile $\mathbf{v}(t)$.

3.1.2. Proposed Rescale Refinement

Starting from the baseline solution ($k = 1$), the algorithm checks whether rescaling is required (Rescaling needed?; Equation (29)). Equation (29) identifies whether the current profile is either constraint-violating (infeasible) or overly conservative, in which case a refinement is triggered. If *No*, the current profile is accepted and the procedure terminates. If *Yes*, the method enters the orange refinement loop in Figure 2 and iteratively updates the phase durations ($k \leftarrow k + 1$) to improve optimality while maintaining compliance with all constraints. After each update, a convergence-based early-stop criterion is evaluated (Early-stop?; Equation (31)) to determine whether further iterations would produce a meaningful change in the phase durations. When the early-stop condition is satisfied, $(\mathbf{a}_1, \mathbf{a}_2)$ are recomputed once using the final durations (rightmost Get $(\mathbf{a}_1, \mathbf{a}_2)$ block), and the procedure terminates; otherwise, the refinement repeats. Consequently, solutions with $k > 1$ correspond to the proposed semi-closed-form solution refined by the rescale loop, yielding a less conservative profile that is closer to near-minimum-time performance under the imposed bounds.

3.2. Kinematics Linearization

This subsection describes the kinematics linearization adopted in prior work [8,17] and refined in the present study. When the quaternion kinematics in Equations (6) and (7) are used directly, the inherent nonlinearities yield a highly coupled relationship between the state variables and the control input. Consequently, it becomes difficult to analytically characterize how variations in the control input affect the quaternion trajectory, which hinders the derivation of closed-form solutions that satisfy the boundary conditions. To alleviate this difficulty, we employ a linearized attitude-kinematics representation in terms of $(\mathbf{q}, \mathbf{v}, \mathbf{a})$:

$$\dot{\mathbf{q}}(t) = \mathbf{v}(t), \tag{10}$$

$$\dot{\mathbf{v}}(t) = \mathbf{a}(t), \tag{11}$$

where $\mathbf{v} \in \mathbb{R}^4$ and $\mathbf{a} \in \mathbb{R}^4$ denote the quaternion velocity and quaternion acceleration, respectively. This representation enables a tractable derivation of boundary-satisfying expressions; the resulting closed-form relations are developed in Section 3.4.

The mapping from $(\mathbf{q}, \boldsymbol{\omega}, \boldsymbol{\alpha})$ to $(\mathbf{q}, \mathbf{v}, \mathbf{a})$ is

$$\mathbf{v} = \dot{\mathbf{q}} = \frac{1}{2}\,\Xi(\mathbf{q})\,\boldsymbol{\omega}, \tag{12}$$

$$\mathbf{a} = \dot{\mathbf{v}} = \frac{1}{2}\,\Xi(\mathbf{v})\,\boldsymbol{\omega} + \frac{1}{2}\,\Xi(\mathbf{q})\,\boldsymbol{\alpha}, \tag{13}$$

where $\Xi(\mathbf{q})$ is defined in Equation (9). For convenience, define the auxiliary vector

$$\mathbf{d} \triangleq \mathbf{a} - \frac{1}{2}\Xi(\mathbf{v})\,\boldsymbol{\omega}. \tag{14}$$

The transformation is used to (i) perform the reference-frame transformation of the boundary conditions (Section 3.3) and (ii) derive a closed-form solution.

Inverse Mapping: Prior Approach vs. Present Approach

After obtaining a semi-closed-form solution in $(\mathbf{q}, \mathbf{v}, \mathbf{a})$, the profiles are mapped back to $(\mathbf{q}, \boldsymbol{\omega}, \boldsymbol{\alpha})$ because the actuator-driven rate and acceleration constraints are defined in the physical variables $(\boldsymbol{\omega}, \boldsymbol{\alpha})$, and the resulting commands must ultimately be expressed in this form for practical implementation. Since $\Xi(\mathbf{q}) \in \mathbb{R}^{4\times 3}$ is non-square, recovering $(\boldsymbol{\omega}, \boldsymbol{\alpha})$ from $(\mathbf{v}, \mathbf{a})$ requires to solve the over-determined equations.

Prior work typically exploited the small-angle regime $q_{d,4} \approx 1$ and used the approximate vector-part relations to form an *explicit* inverse based only on the vector-part mapping (i.e., by inverting a 3×3 submatrix of $\Xi(\mathbf{q})$):

$$\boldsymbol{\omega} \approx 2\big(\Xi_{1:3,\,1:3}(\mathbf{q})\big)^{-1}\mathbf{v}_{1:3}, \qquad \boldsymbol{\alpha} \approx 2\big(\Xi_{1:3,\,1:3}(\mathbf{q})\big)^{-1}\mathbf{d}_{1:3}. \tag{15}$$

While computationally simple and often effective in the small-angle regime, this submatrix-inverse form discards the scalar-part information; consequently, the recovered quantities can be more sensitive to approximation and numerical errors as the small-angle assumption becomes less accurate (e.g., for larger rotations).

In the present study, to consistently combine the above small-angle property with a least-squares-based inverse mapping, we instead employ the Moore–Penrose pseudoinverse of the full matrix $\Xi(\mathbf{q})$ and interpret the recovered quantities as *least-squares* solutions:

$$\boldsymbol{\omega} = 2\big(\Xi(\mathbf{q})\big)^{\dagger}\mathbf{v}, \tag{16}$$

$$\boldsymbol{\alpha} = 2\big(\Xi(\mathbf{q})\big)^{\dagger}\mathbf{d}. \tag{17}$$

Here, $(\Xi(\mathbf{q}))^{\dagger}$ denotes the Moore–Penrose pseudoinverse of $\Xi(\mathbf{q})$, defined as

$$\Xi(\mathbf{q})^{\dagger} \triangleq \big(\Xi(\mathbf{q})^{T}\Xi(\mathbf{q})\big)^{-1}\Xi(\mathbf{q})^{T}, \tag{18}$$

where $\Xi(\mathbf{q}) \in \mathbb{R}^{4\times 3}$ has full column rank for unit quaternions. This construction yields a left-inverse in the least-squares sense and recovers $(\boldsymbol{\omega}, \boldsymbol{\alpha})$ by minimizing the squared residual of the full 4×3 mapping (e.g., $\min_{\omega} \|\Xi(\mathbf{q})\boldsymbol{\omega} - 2\mathbf{v}\|_2^2$). By exploiting all quaternion components, this recovery is typically less sensitive to approximation and numerical errors than a vector-part-only inversion, yielding more reliable estimates of $\boldsymbol{\omega}$ and $\boldsymbol{\alpha}$ for subsequent constraint checks. Consequently, it integrates naturally with the rescale logic—where constraint enforcement is implemented by uniformly scaling the peak levels along the active axis—thereby supporting reliable constraint evaluation within the refinement loop. An ancillary numerical comparison (with the rescale procedure otherwise identical) indicates an approximately 50% improvement in constraint-satisfaction performance when using the pseudoinverse-based mapping instead of the vector-part-only inversion.

The above linearization-based transformation is most accurate when the quaternion difference $\mathbf{q}_d = \mathbf{q}_f \otimes \mathbf{q}_0^{-1}$ satisfies $q_{d,4} \approx 1$ (small principal rotation). As $q_{d,4}$ deviates from unity, the mapping becomes increasingly nonlinear and the approximation error can accumulate through profile construction and kinematics propagation. Accordingly, numerical results from both the prior work and the present study indicate that the termi-

nal mismatch tends to increase noticeably for maneuvers with principal rotation angles exceeding approximately 45°.

3.3. Transformation of Boundary Conditions

This subsection presents a preprocessing step that transforms the boundary conditions into an auxiliary attitude reference frame. To facilitate a closed-form derivation under the kinematics linearization, the boundary conditions are reparameterized in terms of $(\mathbf{q}, \mathbf{v}, \mathbf{a})$. To further mitigate kinematic nonlinearity along the maneuver, we introduce a mid-frame quaternion $\mathbf{q}_{\text{mid}}$ and express the boundary attitudes with respect to this auxiliary frame.

First, define the quaternion difference

$$\mathbf{q}_d = \mathbf{q}_f \otimes \mathbf{q}_0^{-1}, \tag{19}$$

and let $q_{d,4}$ denote its scalar component. The associated eigen-angle and eigen-axis (corresponding to the shortest rotation) are

$$\Delta\theta = 2\cos^{-1}(q_{d,4}), \tag{20}$$

$$\hat{\mathbf{e}} = \mathbf{q}_{d,1:3} / \sin(\Delta\theta/2). \tag{21}$$

Using these, the mid-frame quaternion is defined as

$$\mathbf{q}_{\text{mid}} = \mathbf{q}_{\Delta\theta/2} \otimes \mathbf{q}_0, \tag{22}$$

with

$$\mathbf{q}_{\Delta\theta/2} = \begin{bmatrix} \hat{\mathbf{e}} \sin(\Delta\theta/4) \\ \cos(\Delta\theta/4) \end{bmatrix}. \tag{23}$$

As illustrated in Figure 4, this mid-frame representation symmetrizes the maneuver about $\mathbf{q}_{\text{mid}}$ by mapping the rotation to $\pm\Delta\theta/2$. Consequently, the argument of the $\sin(\cdot)$ relation is shifted toward a lower-curvature region, reducing the impact of nonlinearity and improving the accuracy of the inversion mapping.

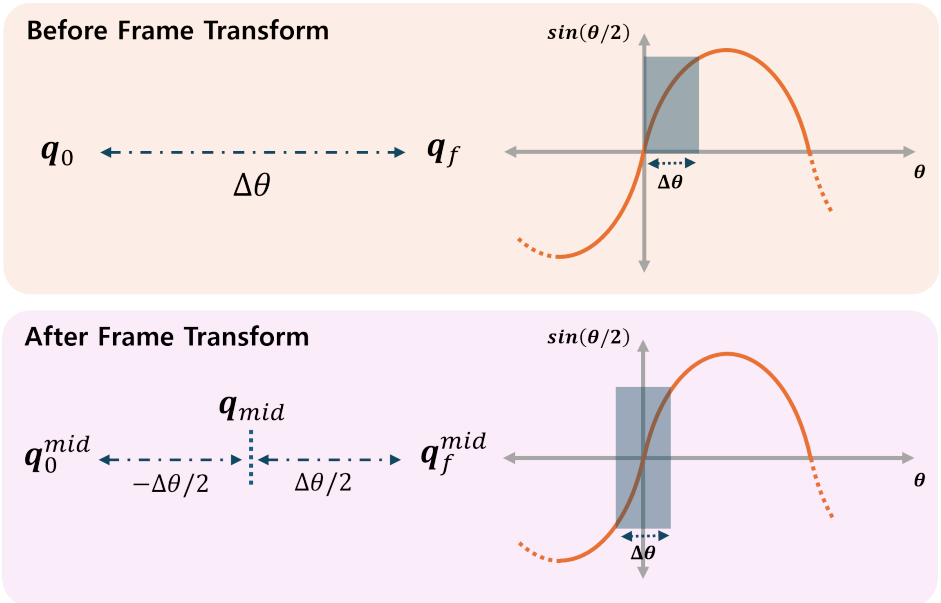


Figure 4. Concept of attitude reference-frame transformation. Top: original initial-to-final rotation $\Delta\theta$. Bottom: mid-frame representation about $\mathbf{q}_{\text{mid}}$ with $\pm\Delta\theta/2$.

The boundary attitudes with respect to the mid-frame are

$$\mathbf{q}_0^{\text{mid}} = \mathbf{q}_0 \otimes \mathbf{q}_{\text{mid}}^{-1}, \tag{24}$$

$$\mathbf{q}_f^{\text{mid}} = \mathbf{q}_f \otimes \mathbf{q}_{\text{mid}}^{-1}, \tag{25}$$

and the corresponding quaternion-velocity boundary terms are obtained as

$$\mathbf{v}_0 = \frac{1}{2}\,\Xi\Big(\mathbf{q}_0^{\text{mid}}\Big)\boldsymbol{\omega}_0, \tag{26}$$

$$\mathbf{v}_f = \frac{1}{2}\,\Xi\Big(\mathbf{q}_f^{\text{mid}}\Big)\boldsymbol{\omega}_f, \tag{27}$$

where $\Xi(\cdot)$ is defined in Equation (9). Once a trajectory $\mathbf{q}^{\text{mid}}(t)$ is obtained in the mid-frame, it is mapped back to the original frame as

$$\mathbf{q}(t) = \mathbf{q}^{\text{mid}}(t) \otimes \mathbf{q}_{\text{mid}}. \tag{28}$$

3.4. Scaling-Based Compensation Method: Rescale Refinement

This subsection describes the scaling-based compensation scheme highlighted in orange in Figure 2. The proposed *rescale* loop is based on the closed-form solution structure within an iterative refinement to (i) recover feasibility when the profile becomes infeasible due to repeated downscaling and (ii) mitigate overly conservative solutions that do not fully utilize the available control authority, thereby reducing the maneuver time while maintaining compliance with the imposed constraints. The following subsections present the loop activation and termination criteria and derive the closed-form rescaling relations associated with the first angular-acceleration constraint, the angular-rate constraint, and the second angular-acceleration constraint, respectively. These relations are implemented in the rescale while-loop to update the maneuver parameters until the prescribed termination condition is satisfied.

3.4.1. Loop Activation and Termination Criteria

In the proposed scaling-based compensation method, the rescale refinement updates the maneuver parameters via a while-loop. This loop is governed by two user-defined thresholds: Threshold_c for the constraint/optimality check and Threshold_t for the termination (convergence) check. To compactly express the loop conditions, define the normalized margins

$$\delta_{\alpha_1} \triangleq \left|\frac{\alpha_{\max,i_s} - \alpha_{1,i_s}}{\alpha_{\max,i_s}}\right|, \quad \delta_{\omega_p} \triangleq \left|\frac{\omega_{\max,i_s} - \omega_{p,i_s}}{\omega_{\max,i_s}}\right|, \quad \delta_{\alpha_2} \triangleq \left|\frac{\alpha_{\max,i_s} - \alpha_{2,i_s}}{\alpha_{\max,i_s}}\right|, \tag{29}$$

where i_s denotes the axis associated with the active (most critical) constraint in the corresponding phase, and α_{1,i_s}, ω_{p,i_s}, and α_{2,i_s} represent the peak values in the first angular-acceleration phase, the angular-rate phase, and the second angular-acceleration phase, respectively. The while-loop is activated if either a feasibility violation occurs or the relative margin exceeds Threshold_c, i.e.,

$$\begin{aligned}&\Big(|\alpha_{1,i_s}| \geq \alpha_{\max,i_s}\Big) \vee \Big(|\omega_{p,i_s}| \geq \omega_{\max,i_s}\Big) \vee \\ &\Big(|\alpha_{2,i_s}| \geq \alpha_{\max,i_s}\Big) \vee \Big(\max\{\delta_{\alpha_1}, \delta_{\omega_p}, \delta_{\alpha_2}\} \geq \text{Threshold}_c\Big).\end{aligned} \tag{30}$$

To prevent excessive iterations, the while-loop is terminated when the relative changes in the updated phase durations become sufficiently small. Let $(\cdot)^-$ and $(\cdot)^+$ denote the values *before* and *after* a rescaling update, and define

$$\varepsilon_{\alpha_1} \triangleq \left| \frac{t_{\alpha_1}^+ - t_{\alpha_1}^-}{t_{\alpha_1}^-} \right|, \quad \varepsilon_{\omega_p} \triangleq \left| \frac{t_{\omega_p}^+ - t_{\omega_p}^-}{t_{\omega_p}^-} \right|, \quad \varepsilon_{\alpha_2} \triangleq \left| \frac{t_{\alpha_2}^+ - t_{\alpha_2}^-}{t_{\alpha_2}^-} \right|. \tag{31}$$

The termination condition is then given by

$$\max\{\varepsilon_{\alpha_1}, \varepsilon_{\omega_p}, \varepsilon_{\alpha_2}\} \leq \text{Threshold}_t. \tag{32}$$

When Equation (32) is satisfied, the rescale loop is regarded as converged and the while-loop is stopped.

3.4.2. Rescaling Equations for the First Angular-Acceleration Constraint

This subsection derives the rescaling relation associated with the first angular-acceleration constraint. Since the hardware limits are specified in the original variables $(\mathbf{q}, \boldsymbol{\omega}, \boldsymbol{\alpha})$, they cannot be imposed directly in the linearized parameterization $(\mathbf{q}, \mathbf{v}, \mathbf{a})$. Accordingly, at each rescale iteration the current $(\mathbf{q}, \mathbf{v}, \mathbf{a})$ is mapped back to $(\mathbf{q}, \boldsymbol{\omega}, \boldsymbol{\alpha})$, and the rescaling is performed by exploiting the small-angle proportionalities $\mathbf{v}_{1:3} \propto \boldsymbol{\omega}$ and $\mathbf{a}_{1:3} \propto \boldsymbol{\alpha}$. To enforce (or more fully utilize) the available acceleration authority, the first angular-acceleration segment is updated using a uniform scaling factor determined by the limiting axis:

$$\mathbf{a}_1^+ \leftarrow \left(\frac{\alpha_{\max,i_s^\star}}{|\alpha_{1,i_s^\star}|} \right) \mathbf{a}_1^-, \tag{33}$$

$$i_s^\star = \arg \min_{i \in \{1,2,3\}} \frac{\alpha_{\max,i}}{|\alpha_{1,i}|}, \tag{34}$$

where $i_s^\star$ denotes the active (limiting) axis. Specifically, $i_s^\star$ corresponds to the axis closest to saturation in an overly conservative case and to the axis with the largest constraint violation in an infeasible case. This unified selection enables both *down-scaling* (to recover feasibility when a constraint is violated) and *up-scaling* (to compensate overly conservative solutions by tightening the constraint margin), while ensuring that the rescaled profile does not exceed the hardware bound on any axis.

Once the rescale refinement loop is entered, the profile structure is assumed to be fixed by the preceding steps. As illustrated in Figure 3, the maneuver is represented by a unified parameterization, and the realized profile type is determined by whether the intermediate coasting duration becomes degenerate. In particular, when the coasting duration vanishes (i.e., $t_{\omega_p} = 0$), the intermediate zero-acceleration segment disappears and the nominal bang–off–bang structure reduces to a bang–bang profile with a direct transition from acceleration to deceleration. Accordingly, the proposed rescale logic operates within the same unified parameterization, while allowing the profile to simplify to either bang–off–bang or bang–bang depending on whether t_{ω_p} is nonzero or zero. For completeness, the closed-form update rules in the subsequent subsections are derived so that they remain well-defined even in the degenerate case $t_{\omega_p} = 0$ (bang–bang reduction). If the intermediate coasting segment is absent, the angular-rate rescaling becomes inapplicable, while the same update logic remains applicable to the remaining phases (e.g., the deceleration segment) without

introducing additional case-specific derivations. Under the linearized kinematics and the adopted profile parameterization, the boundary conditions yield

$$\mathbf{v}_f = \mathbf{v}_0 + \mathbf{a}_1 t_r + \mathbf{a}_2 t_r, \tag{35}$$

$$\mathbf{q}_f^{\text{mid}} = \mathbf{q}_0^{\text{mid}} + \frac{1}{2}\Big(\mathbf{v}_0 + \mathbf{v}_p\Big)(t_r + t_{\alpha_1}) + \mathbf{v}_p t_{\omega_p} + \frac{1}{2}\Big(\mathbf{v}_p + \mathbf{v}_f\Big)(t_r + t_{\alpha_2}). \tag{36}$$

Substituting the updated $\mathbf{a}_1$ from Equation (33) into Equations (35) and (36) yields a quadratic equation in t_{α_1}:

$$A\, t_{\alpha_1}^2 + B\, t_{\alpha_1} + C = 0, \tag{37}$$

with coefficients

$$A = \frac{1}{2}\, a_{1,i_s^\star}, \tag{38}$$

$$B = v_{0,i_s^\star} + \frac{1}{2}\, a_{1,i_s^\star}\Big(5t_r + 2t_{\omega_p} + t_{\alpha_2}\Big), \tag{39}$$

$$\begin{aligned} C = {} & q_{0,i_s^\star}^{\text{mid}} - q_{f,i_s^\star}^{\text{mid}} + \frac{1}{2}\, v_{0,i_s^\star}\Big(6t_r + 2t_{\omega_p} + t_{\alpha_2}\Big) \\ & + \frac{1}{2}\, a_{1,i_s^\star}\Big(3t_r^2 + 2t_r t_{\omega_p} + t_r t_{\alpha_2}\Big) + \frac{1}{2}\, v_{f,i_s^\star}(2t_r + t_{\alpha_2}). \end{aligned} \tag{40}$$

Thus, t_{α_1} is updated via

$$t_{\alpha_1} \leftarrow \frac{-B \pm \sqrt{B^2 - 4AC}}{2A}. \tag{41}$$

Among the two roots, the physically admissible solution is selected to satisfy $t_{\alpha_1} \geq 0$ and to preserve consistency with the assumed profile structure.

Note that both the scaling in Equation (33) and the update of t_{α_1} in Equation (41) are determined by the active axis $i_s^\star$, which corresponds to the most critical constraint direction. Accordingly, t_{α_1} is updated to reduce the dominant constraint discrepancy along $i_s^\star$. After updating t_{α_1}, the quaternion-linearized profile parameters are recomputed to ensure that the boundary relations in Equations (35) and (36) hold for all components. Specifically, $\mathbf{a}_1$, $\mathbf{a}_2$, and $\mathbf{v}_p$ are recalculated as

$$\mathbf{a}_1 = \frac{\mathbf{v}_p - \mathbf{v}_0}{t_r + t_{\alpha_1}}, \tag{42}$$

$$\mathbf{a}_2 = \frac{\mathbf{v}_f - \mathbf{v}_p}{t_r + t_{\alpha_2}}. \tag{43}$$

$$\mathbf{v}_p = \frac{\mathbf{q}_f^{\text{mid}} - \mathbf{q}_0^{\text{mid}} - \mathbf{v}_0\Big(t_r + \frac{t_{\alpha_1}}{2}\Big) - \mathbf{v}_f\Big(t_r + \frac{t_{\alpha_2}}{2}\Big)}{2t_r + \frac{1}{2}t_{\alpha_1} + t_{\omega_p} + \frac{1}{2}t_{\alpha_2}}. \tag{44}$$

These updates restore consistency between the rescaled phase durations and the quaternion-linearized boundary conditions, thereby yielding a feasible maneuver profile that conforms to the adopted parameterization.

3.4.3. Rescaling Equations for the Angular-Rate Constraint

This subsection describes the rescaling procedure associated with the angular-rate constraint. To update the constant-rate duration t_{ω_p} while enforcing (or more fully utilizing) the angular-rate bound, the peak quaternion velocity $\mathbf{v}_p$ is first rescaled as

$$\mathbf{v}_p \leftarrow \left(\frac{\omega_{\max,i_s^\star}}{\left|\omega_{p,i_s^\star}\right|}\right)\mathbf{v}_p, \tag{45}$$

where the active (limiting) axis index $i_s^\star$ is selected as

$$i_s^\star = \arg\min_{i\in\{1,2,3\}} \frac{\omega_{\max,i}}{|\omega_{p,i}|}. \tag{46}$$

Since the change in $\mathbf{v}_p$ affects both acceleration and deceleration phases, a consistent update generally requires modifying not only t_{ω_p} but also t_{α_1} and t_{α_2}. Given that the profile structure is fixed by the preceding steps, we update t_{α_1} and t_{α_2} using the axes that exhibit the largest quaternion-velocity variations:

$$i_{t\alpha_1}^\star = \arg\max_{i\in\{1,2,3\}} \left|v_{p,i} - v_{0,i}\right|, \tag{47}$$

$$i_{t\alpha_2}^\star = \arg\max_{i\in\{1,2,3\}} \left|v_{f,i} - v_{p,i}\right|. \tag{48}$$

The corresponding phase durations are then updated as

$$t_{\alpha_1} = \frac{v_{p,i_{t\alpha_1}^\star} - v_{0,i_{t\alpha_1}^\star} - a_{1,i_{t\alpha_1}^\star} t_r}{a_{1,i_{t\alpha_1}^\star}}, \tag{49}$$

$$t_{\alpha_2} = \frac{v_{f,i_{t\alpha_2}^\star} - v_{p,i_{t\alpha_2}^\star} - a_{2,i_{t\alpha_2}^\star} t_r}{a_{2,i_{t\alpha_2}^\star}}. \tag{50}$$

This selection yields conservative phase-duration updates by referencing the axis requiring the largest change in quaternion velocity.

Finally, t_{ω_p} is obtained in closed form as

$$t_{\omega_p} = \frac{q_{f,i_s^\star}^{\mathrm{mid}} - q_{p,i_s^\star}^{\mathrm{mid}} - \frac{1}{2}\left(v_{p,i_s^\star} + v_{f,i_s^\star}\right)(2t_r + t_{\alpha_2})}{v_{p,i_s^\star}}, \tag{51}$$

where $q_{p,i_s^\star}^{\mathrm{mid}}$ denotes the $i_s^\star$-th component of $\mathbf{q}_p^{\mathrm{mid}}$, i.e., the mid-frame quaternion at the instant when the quaternion velocity first reaches $\mathbf{v}_p$ (the end of the first angular-acceleration phase). Note that $v_{p,i_s^\star}$ in Equation (51) is the value obtained from the updated phase durations (in particular, the updated t_{α_1}), rather than the directly rescaled $\mathbf{v}_p$ in Equation (45).

After updating $(t_{\alpha_1}, t_{\omega_p}, t_{\alpha_2})$, the quantities $\mathbf{a}_1$, $\mathbf{a}_2$, and $\mathbf{v}_p$ are recomputed using Equations (42)–(44), thereby restoring consistency with the adopted profile parameterization.

3.4.4. Rescaling Equations for the Second Angular-Acceleration Constraint

This subsection describes the rescaling procedure associated with the second angular-acceleration constraint. Similar to the update of $\mathbf{a}_1$, the deceleration angular-acceleration vector $\mathbf{a}_2$ is uniformly rescaled using the active (limiting) axis:

$$\mathbf{a}_2 \leftarrow \left(\frac{\alpha_{\max,i_s^\star}}{|\alpha_{2,i_s^\star}|}\right)\mathbf{a}_2, \tag{52}$$

where the active axis index $i_s^\star$ is selected by

$$i_s^\star = \arg\min_{i\in\{1,2,3\}} \frac{\alpha_{\max,i}}{|\alpha_{2,i}|}. \tag{53}$$

Here, $i_s^\star$ denotes the active (limiting) axis; it is the axis closest to saturation in the overly conservative case and the axis with the largest constraint violation in the infeasible case.

Substituting the updated $\mathbf{a}_2$ into the boundary-consistent relations yields a quadratic equation in t_{α_2}, whose solution is

$$t_{\alpha_2} \leftarrow \frac{-E \pm \sqrt{E^2 - 4DF}}{2D}, \tag{54}$$

with coefficients

$$D = -\frac{1}{2} a_{2,i_s^\star}, \tag{55}$$

$$E = v_{f,i_s^\star} - a_{2,i_s^\star}\left(2.5t_r + 0.5t_{\alpha_1} + t_{\omega_p}\right), \tag{56}$$

$$F = \left(q_{0,i_s^\star}^{\text{mid}} - q_{f,i_s^\star}^{\text{mid}}\right) + \left(v_{0,i_s^\star} t_r + \frac{1}{2} v_{0,i_s^\star} t_{\alpha_1} + v_{f,i_s^\star} t_r\right) + \left(v_{f,i_s^\star} - a_{2,i_s^\star} t_r\right)\left(2t_r + \frac{1}{2} t_{\alpha_1} + t_{\omega_p}\right). \tag{57}$$

Among the two roots, the physically admissible solution is selected to satisfy $t_{\alpha_2} \geq 0$ and to preserve consistency with the assumed profile structure.

After updating t_{α_2}, the quantities $\mathbf{a}_1$, $\mathbf{a}_2$, and $\mathbf{v}_p$ are recomputed using Equations (42)–(44), thereby restoring consistency with the adopted profile parameterization.

4. Numerical Results

This section presents numerical studies to assess the effectiveness of the semi-closed-form solution. First, the proposed method is compared with the baseline (reference) method using representative test cases to demonstrate its ability to (i) recover feasibility in constraint-violating scenarios and (ii) mitigate conservatism in overly conservative scenarios via improved optimality. Next, Monte Carlo (MC) simulations provide quantitative comparisons: the proposed method is evaluated against the baseline in terms of constraint satisfaction, optimality, and computation time, and it is further compared with a numerical minimum-time solver in terms of terminal attitude accuracy and maneuver-time characteristics. Finally, to bridge the gap between open-loop command generation and practical spacecraft operation, the profiles produced by the semi-closed-form solution are embedded in a feedforward–feedback structure, illustrating that the generated commands can be deployed in a closed-loop setting while maintaining the desired terminal performance.

4.1. Baseline Method vs. the Semi-Closed-Form Solution

4.1.1. Case I: Infeasible Solution

This case demonstrates the feasibility-recovery capability of the semi-closed-form solution when the baseline method yields an infeasible maneuver profile. The simulation conditions (boundary conditions and constraints) are summarized in Table 1. Figures 5 and 6 illustrate the maneuver profiles generated by the baseline and proposed methods, respectively. As shown in Figure 5, although the baseline solution satisfies the boundary conditions, it violates the angular-acceleration bound during the first acceleration phase (see Figure 5d); hence, the resulting maneuver is infeasible with respect to the imposed constraints.

In contrast, the proposed method incorporates the proposed rescale step to update the maneuver parameters such that all constraints are satisfied while preserving the prescribed profile structure. As shown in Figure 6, the rescaled solution remains within the angular-rate and angular-acceleration bounds (red horizontal lines) and simultaneously maintains boundary-condition satisfaction. Moreover, the maneuver duration is reduced from 19.2 s (baseline) to 18.4 s (semi-closed-form solution) after feasibility recovery. Overall, this case

indicates that the proposed refinement can recover feasibility while maintaining boundary-condition compliance and reducing maneuver time.

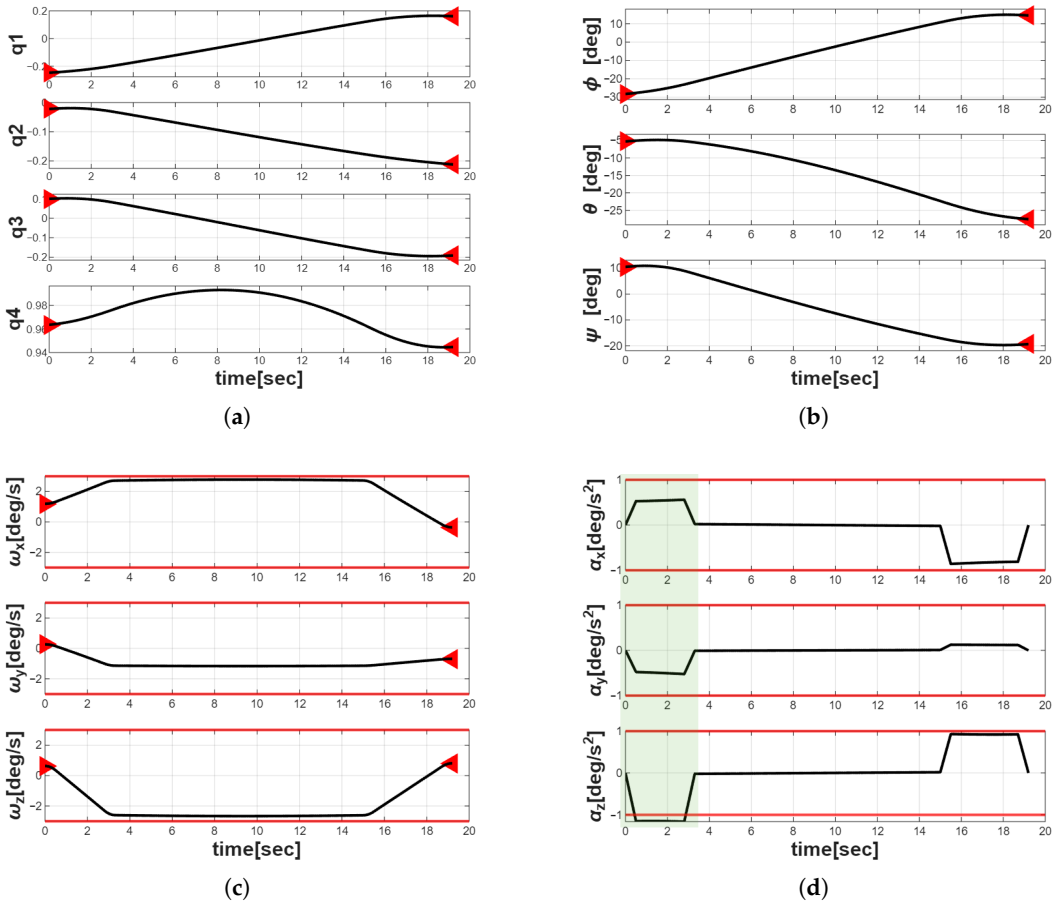


Figure 5. Attitude maneuver profiles obtained by the **baseline method** for the **infeasible case**: (**a**) quaternion trajectory $\mathbf{q}(t)$; (**b**) Euler-angle trajectory $(\phi(t), \theta(t), \psi(t))$; (**c**) angular-rate profile $\boldsymbol{\omega}(t)$; (**d**) angular-acceleration profile $\boldsymbol{\alpha}(t)$. The red horizontal lines indicate the corresponding bounds, and the baseline solution violates the angular-acceleration constraint in the first acceleration phase.

Table 1. Simulation conditions for Case I.

Category	Quantity	Value
Boundary conditions	$\boldsymbol{\theta}_0$ [deg]	$[-28.29, \ -5.27, \ \ 10.49]^T$
	$\boldsymbol{\omega}_0$ [deg/s]	$[\ \ 1.191, \ \ 0.266, \ \ 0.633]^T$
	$\boldsymbol{\theta}_f$ [deg]	$[\ \ 14.56, -27.55, -19.33]^T$
	$\boldsymbol{\omega}_f$ [deg/s]	$[-0.360, -0.686, \ \ 0.809]^T$
Constraints/parameter	$\alpha_{\max}$ [deg/s^2]	1
	$\omega_{\max}$ [deg/s]	3
	t_r [s]	0.5

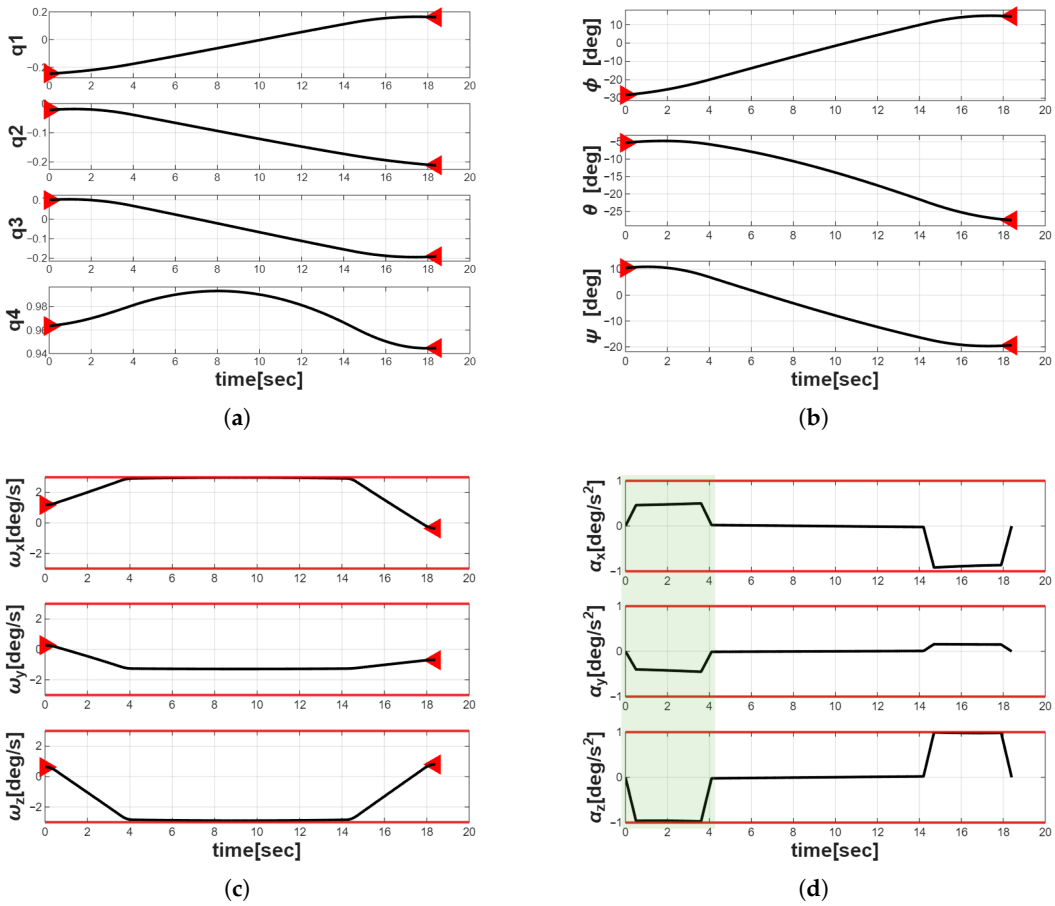


Figure 6. Attitude maneuver profiles obtained by the **semi-closed-form solution** for the **infeasible case** after feasibility recovery: (**a**) quaternion trajectory $\mathbf{q}(t)$; (**b**) Euler-angle trajectory $(\phi(t), \theta(t), \psi(t))$; (**c**) angular-rate profile $\boldsymbol{\omega}(t)$; (**d**) angular-acceleration profile $\boldsymbol{\alpha}(t)$. The red horizontal lines indicate the corresponding bounds, and the rescale step restores feasibility while preserving the prescribed profile structure.

4.1.2. Case II: Overly Conservative Solution

This case demonstrates the conservatism-mitigation capability of the semi-closed-form solution when the baseline method yields an overly conservative profile that underutilizes the available control authority. The simulation conditions are summarized in Table 2. Figures 7 and 8 illustrate the maneuver profiles produced by the baseline and proposed methods, respectively. In both cases, the generated trajectories satisfy the prescribed boundary conditions (initial/terminal attitudes and angular rates). However, as shown in Figure 7, the baseline solution remains well within the angular-rate bound, indicating excessive conservatism and insufficient utilization of the allowable limits. This conservative scaling yields a longer maneuver time than necessary despite feasibility.

By contrast, Figure 8 shows that the proposed method applies the iterative rescale refinement to raise the peak angular rate toward its bound while preserving feasibility and satisfying the same boundary conditions. As a result, the maneuver time is reduced from 10.2 s (baseline) to 9.6 s (semi-closed-form solution), yielding a less conservative profile driven closer to a near-minimum-time solution under the prescribed constraints.

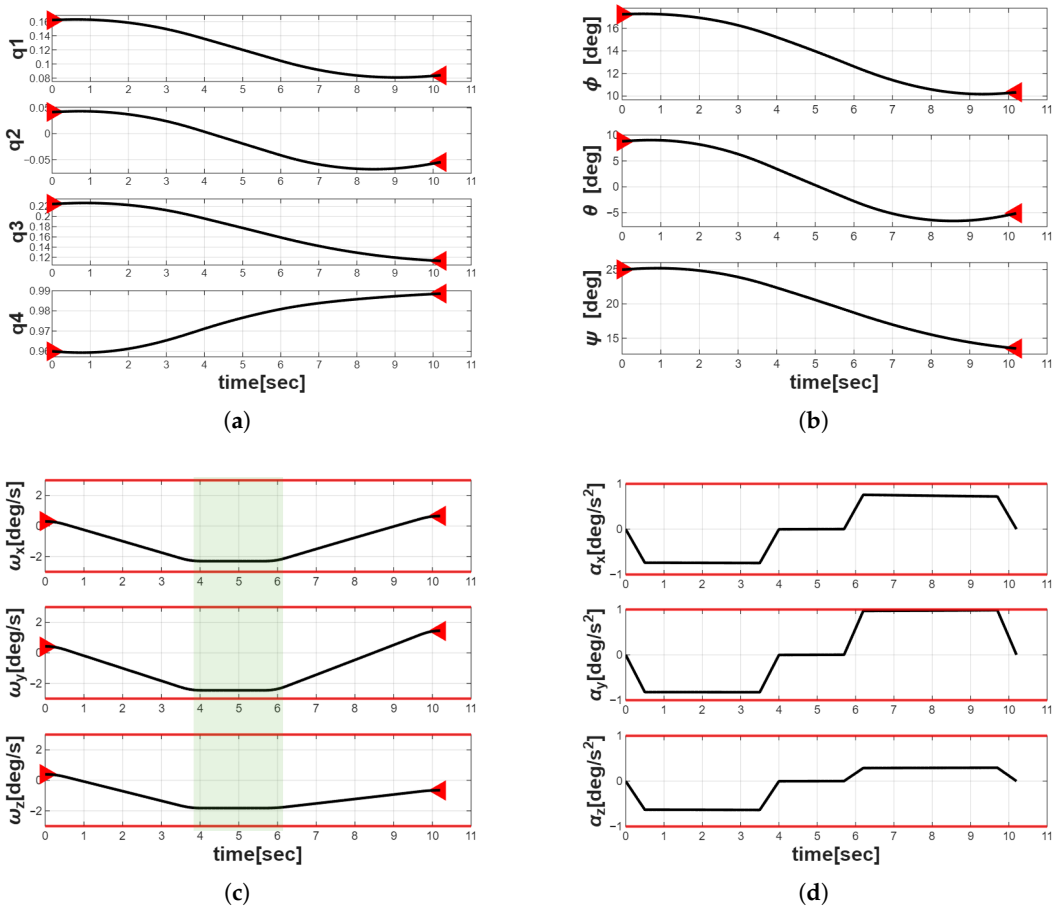


Figure 7. Attitude maneuver profiles obtained by the **baseline method** for the **overly conservative case**: (**a**) quaternion trajectory $\mathbf{q}(t)$; (**b**) Euler-angle trajectory $(\phi(t), \theta(t), \psi(t))$; (**c**) angular-rate profile $\boldsymbol{\omega}(t)$; (**d**) angular-acceleration profile $\boldsymbol{\alpha}(t)$. The red horizontal lines indicate the corresponding bounds. Although the baseline solution satisfies the boundary conditions and remains feasible, the peak angular rate stays well below $\omega_{\max}$, indicating excessive conservatism (underutilization of the available limits) and consequently a longer maneuver time than necessary.

Table 2. Simulation conditions for Case II.

Category	Quantity	Value
Boundary conditions	$\boldsymbol{\theta}_0$ [deg]	$[\ 17.24,\ \ 8.79,\ \ 24.98]^T$
	$\boldsymbol{\omega}_0$ [deg/s]	$[\ 0.302,\ \ 0.427,\ \ 0.396]^T$
	$\boldsymbol{\theta}_f$ [deg]	$[\ 10.33,\ -5.13,\ \ 13.49]^T$
	$\boldsymbol{\omega}_f$ [deg/s]	$[-0.657,\ \ 1.451,\ -0.648]^T$
Constraints/parameter	$\alpha_{\max}$ [deg/s^2]	1
	$\omega_{\max}$ [deg/s]	3
	t_r [s]	0.5

4.1.3. Monte Carlo Results: Baseline vs. Semi-Closed-Form Solution

This subsection quantitatively compares the baseline and proposed methods using an MC simulation. For each trial, random boundary conditions are generated according to Table 3, and both methods are executed under identical constraint bounds and algorithmic settings. The resulting maneuver profiles are evaluated using the performance indices defined below, which assess (i) constraint feasibility, (ii) degree of enhanced optimality (as a proxy for near-minimum-time behavior), and (iii) computational efficiency.

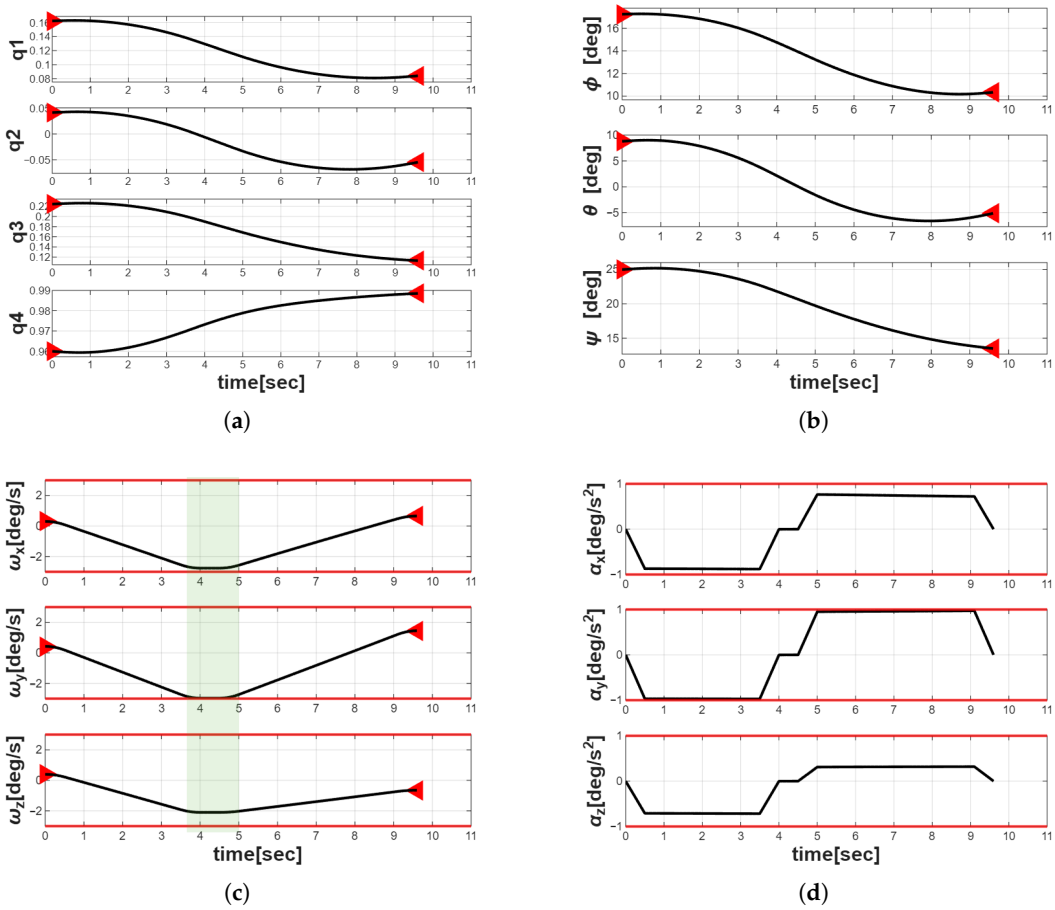


Figure 8. Attitude maneuver profiles obtained by the **semi-closed-form solution** for the **overly conservative case**: (**a**) quaternion trajectory $\mathbf{q}(t)$; (**b**) Euler-angle trajectory $(\phi(t), \theta(t), \psi(t))$; (**c**) angular-rate profile $\boldsymbol{\omega}(t)$; (**d**) angular-acceleration profile $\boldsymbol{\alpha}(t)$. The red horizontal lines indicate the corresponding bounds. In contrast to the baseline solution, the rescale step increases the peak angular rate toward $\omega_{\max}$ (i.e., improves optimality) while preserving feasibility and satisfying the same boundary conditions, thereby yielding a less conservative profile.

Table 3. Monte Carlo simulation conditions.

Category	Quantity	Value
Boundary conditions (random)	$\boldsymbol{\theta}_0$ [deg]	$[-60, 60]$ (Each component uniformly sampled)
	$\boldsymbol{\omega}_0$ [deg/s]	$[-15, 15]$ (Each component uniformly sampled)
	$\boldsymbol{\theta}_f$ [deg]	$[-60, 60]$ (Each component uniformly sampled)
	$\boldsymbol{\omega}_f$ [deg/s]	$[-15, 15]$ (Each component uniformly sampled)
Constraints/parameter	$\alpha_{\max}$ [deg/s^2]	1
	$\omega_{\max}$ [deg/s]	3
	t_r [s]	0.5
Simulation setup	N_{simul}	10,000
	Threshold$_c$	1×10^{-10}
	Threshold$_t$	1×10^{-20}
	ε_{sat}	0.005

Performance Indices

- Constraint satisfaction (CS)

$$\mathrm{CS} \triangleq \mathbb{I}\Big[\big(|\alpha_{1,i_s}| \le \alpha_{\max,i_s}\big) \wedge \big(|\omega_{p,i_s}| \le \omega_{\max,i_s}\big) \wedge \big(|\alpha_{2,i_s}| \le \alpha_{\max,i_s}\big)\Big].$$

(Satisfying: 1, Unsatisfying: 0).

- Constraint-boundary proximity (CP)

$$\mathrm{CP} \triangleq \mathbb{I}\Big[\min\Big\{\frac{|\alpha_{\max,i_s} - |\alpha_{1,i_s}||}{\alpha_{\max,i_s}}, \frac{|\omega_{\max,i_s} - |\omega_{p,i_s}||}{\omega_{\max,i_s}}, \frac{|\alpha_{\max,i_s} - |\alpha_{2,i_s}||}{\alpha_{\max,i_s}}\Big\} \le \varepsilon_{\mathrm{CP}}\Big].$$

(Within tolerance: 1, Outside tolerance: 0).

- Constraint margin (CM)

$$\mathrm{CM} \triangleq \frac{|\alpha_{\max,i_s} - |\alpha_{1,i_s}||}{\alpha_{\max,i_s}} + \frac{|\omega_{\max,i_s} - |\omega_{p,i_s}||}{\omega_{\max,i_s}} + \frac{|\alpha_{\max,i_s} - |\alpha_{2,i_s}||}{\alpha_{\max,i_s}}.$$

(smaller CM indicates higher optimality).

- Computation time (CT)

$$\mathrm{CT}: \text{ wall-clock time per trial.}$$

(Hardware: AMD Ryzen 7 5800HS, RAM 16 GB.)

Here, α_{1,i_s}, ω_{p,i_s}, and α_{2,i_s} denote the peak values (along the active axis i_s) associated with the first angular-acceleration phase, the angular-rate phase, and the second angular-acceleration phase, respectively, and $\alpha_{\max,i_s}$ and $\omega_{\max,i_s}$ denote the corresponding bounds. The function $\mathbb{I}[\cdot]$ is the indicator function and $\varepsilon_{\mathrm{CP}}$ is the proximity tolerance, set to $\varepsilon_{\mathrm{CP}} = 0.005$ in this work. Isotropic bounds are assumed, i.e., $\alpha_{\max,i_s} = \alpha_{\max}$ and $\omega_{\max,i_s} = \omega_{\max}$ for $i_s \in \{1,2,3\}$. If a phase duration becomes zero (i.e., $t_{\alpha_1} = 0$, $t_{\omega_p} = 0$, or $t_{\alpha_2} = 0$), the corresponding phase-wise CM term is set to zero by definition.

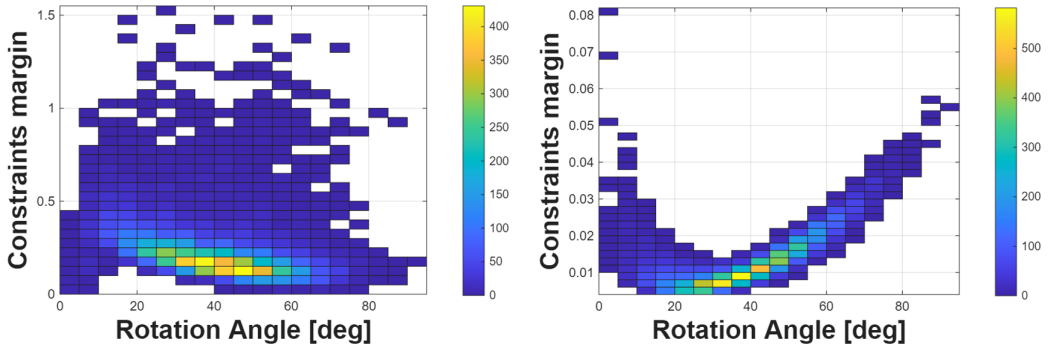
Monte Carlo Results and Discussion

Table 4 summarizes the Monte Carlo (MC) comparison between the baseline and proposed methods using CS, CP, CM, and CT. With the exception of CT, the proposed semi-closed-form method achieves better performance than the baseline. In particular, the number of constraint-satisfying trials increases from 3259 to 6427 (an improvement of approximately 97%), indicating a substantial reduction in infeasible solutions. In terms of constraint-boundary proximity (limit utilization), the proposed method achieves CP = 10,000/10,000, indicating that all trials satisfy the prescribed proximity-tolerance criterion with respect to the active constraint, whereas the baseline achieves 6212 such trials. Moreover, the average constraint margin decreases from 0.21974 to 0.01266 (about a 94.2% reduction), implying that the proposed method operates much closer to the available bounds and is, therefore, driven toward near-minimum-time maneuvers. Figure 9 visualizes CM as a function of the rotation angle. For the baseline method (Figure 9a), CM values are broadly dispersed, indicating that a non-negligible portion of trials substantially underutilizes the allowable bounds. In contrast, the proposed method (Figure 9b) yields a markedly concentrated CM distribution, with the bins corresponding to CM $\le$ 0.05 being densely populated. This concentration indicates that the rescale step systematically mitigates conservatism by driving the solutions toward the boundary of the active constraint across the MC set. The computation-time scatter in Figure 10 highlights the additional computational cost incurred by the proposed method. The baseline method (Figure 10a) typically completes with negligible runtime per trial, whereas the proposed method (Figure 10b) exhibits increased wall-clock time due to the iterative rescale-based recalibration (about 26 iterations on average). Accordingly, the mean computation time increases from 0.00016 s to 0.00660 s per trial (roughly $> 40\times$). Nevertheless, the resulting mean runtime of 6.60 ms may be

acceptable for on-board use under typical computational budgets, particularly given the pronounced improvements in feasibility recovery and optimality.

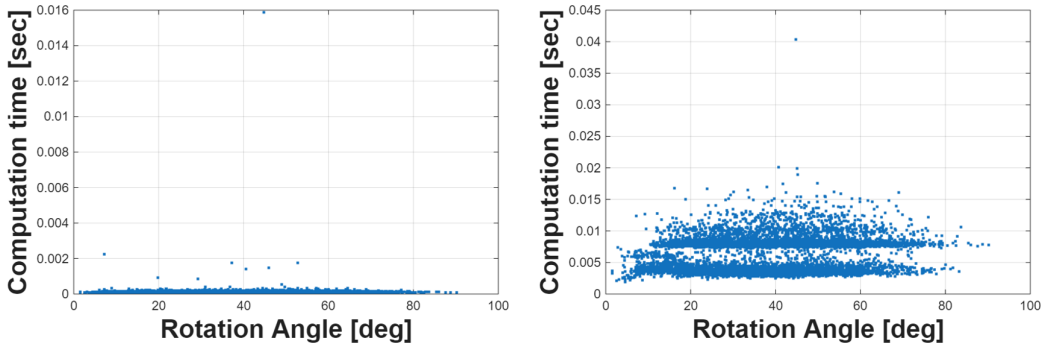
Table 4. Monte Carlo simulation results (baseline vs. semi-closed-form solution).

Performance Indices	Baseline	Semi-Closed-Form
Constraint satisfaction (CS)	3259	6427
Constraint-boundary proximity (CP)	6212	10,000
Constraint margin (CM) [avg.]	0.21974	0.01266
Computation time (CT) [avg., s]	0.00016	0.00660



(**a**) (**b**)

Figure 9. Constraint-margin (CM) distribution versus rotation angle obtained from the Monte Carlo simulation: (**a**) baseline method and (**b**) semi-closed-form solution. The colorbar indicates the number of samples in each bin.



(**a**) (**b**)

Figure 10. Computation time versus rotation angle obtained from the Monte Carlo simulation: (**a**) baseline method and (**b**) semi-closed-form solution. Each marker corresponds to one trial, and the vertical axis shows the wall-clock computation time per trial.

4.2. Semi-Closed-Form Solution vs. Numerical Optimization-Based Solution (Monte Carlo)

This subsection evaluates the semi-closed-form solution against a numerical optimization-based method via an MC simulation. The comparison focuses on (i) terminal attitude-matching quality obtained by propagating the attitude kinematics under the semi-closed-form command profiles and (ii) maneuver-time discrepancy relative to the numerically optimized solution. Unless otherwise stated, the horizontal axis (rotation angle) denotes the principal rotation angle implied by the prescribed boundary conditions for each trial. The MC conditions are summarized in Table 3, which are identical to those used in the baseline method–proposed method comparison.

4.2.1. Numerical Minimum-Time Problem

To enable a direct comparison, the numerical solver is configured to minimize maneuver time subject to the same kinematic model and box-shaped, hardware-driven constraints used throughout this paper. The angular-acceleration command is parameterized as a jerk-limited bang–off–bang profile with a fixed transition time t_r, and the decision variables are collected in

$$\boldsymbol{x} \triangleq \left[\, t_{a_1},\ t_{\omega_p},\ t_{a_2},\ \boldsymbol{\alpha}_1^T,\ \boldsymbol{\alpha}_2^T \,\right]^T,$$

where t_{a_1}, t_{ω_p}, and t_{a_2} follow the same definitions and notation as in the proposed semi-closed-form solution, and $\boldsymbol{\alpha}_1$ and $\boldsymbol{\alpha}_2$ denote the constant angular-acceleration levels in the acceleration and deceleration phases, respectively. With the fixed transition time t_r, the total maneuver time is

$$t_f = t_{a_1} + t_{\omega_p} + t_{a_2} + 4t_r. \tag{58}$$

Because t_r is fixed, minimizing t_f is equivalent to minimizing $t_{a_1} + t_{\omega_p} + t_{a_2}$. Accordingly, the numerical minimum-time problem is formulated as

$$\begin{aligned}
\min_{\boldsymbol{x}} \quad & J(\boldsymbol{x}) = t_{a_1} + t_{\omega_p} + t_{a_2} \\
\text{s.t.} \quad & \dot{\mathbf{q}}(t) = \tfrac{1}{2}\,\Xi(\mathbf{q}(t))\,\boldsymbol{\omega}(t), \\
& \dot{\boldsymbol{\omega}}(t) = \boldsymbol{\alpha}(t), \\
& \boldsymbol{\alpha}(t) = \boldsymbol{\alpha}(t;\boldsymbol{x}), \qquad t \in [0, t_f], \\
& \mathbf{q}(0) = \mathbf{q}_0,\ \boldsymbol{\omega}(0) = \boldsymbol{\omega}_0,\ \mathbf{q}(t_f) = \mathbf{q}_f,\ \boldsymbol{\omega}(t_f) = \boldsymbol{\omega}_f, \\
& |\omega_i(t)| \le \omega_{\max,i}, \quad |\alpha_i(t)| \le \alpha_{\max,i}, \quad i = 1,2,3.
\end{aligned} \tag{59}$$

The nonlinear optimization problem is solved in MATLAB R2025a using `fmincon` with the SQP algorithm; the baseline solution is provided as the initial guess to enhance convergence robustness.

4.2.2. Performance Indices

The following indices quantify the discrepancy between the semi-closed-form solution and the numerical solution.

- Attitude error (AE)

$$\theta_{\text{err}} \triangleq 2\cos^{-1}(q_{d,4}), \qquad \mathbf{q}_d = \mathbf{q}_f \otimes \mathbf{q}_{\text{terminal}}^{-1}.$$

  (smaller is better; $\theta_{\text{err}} = 0$ indicates perfect terminal-attitude matching).
- Maneuver-time deviation (MTD)

$$\Delta T \triangleq T_{\text{semi}} - T_{\text{num}}.$$

  ($\Delta T < 0$: faster than the numerical solution; $\Delta T > 0$: slower).

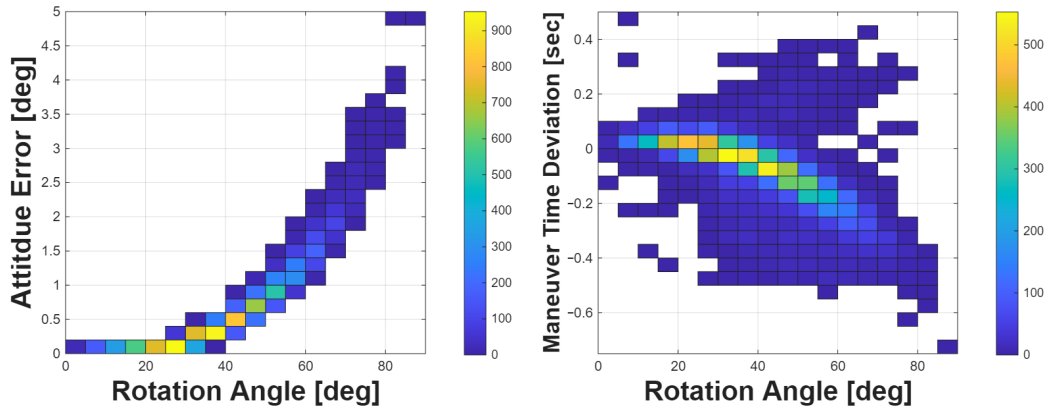
Here, $\mathbf{q}_{\text{terminal}}$ denotes the terminal attitude quaternion reconstructed by propagating the quaternion kinematics using the semi-closed-form solution's angular-acceleration profile $\boldsymbol{\alpha}(t)$ (i.e., $\boldsymbol{\alpha}(t) \to \boldsymbol{\omega}(t) \to \mathbf{q}(t)$, evaluated at $t = t_f$). The prescribed terminal quaternion is $\mathbf{q}_f$, and $\otimes$ denotes quaternion multiplication. The scalar component of $\mathbf{q}_d$ is $q_{d,4}$ under the ordering $\mathbf{q} = [q_1\ q_2\ q_3\ q_4]^T$.

4.2.3. Monte Carlo Results and Discussion

Figure 11 summarizes the MC results in terms of the above indices. As shown in Figure 11a, the attitude error tends to increase with the rotation angle. For rotation angles up to approximately 50°, the proposed method typically achieves $\theta_{\text{err}} \le 1°$, while the terminal mismatch becomes more noticeable for larger rotations. This trend is expected because

the semi-closed-form solution is generated based on a linearized boundary-condition transformation, which yields reference profiles consistent with the kinematic linearization. When the resulting angular-acceleration profile $\boldsymbol{\alpha}(t)$ is used to reconstruct the terminal attitude through kinematics propagation, the propagated terminal quaternion $\mathbf{q}_{\text{terminal}}$ can deviate from the desired $\mathbf{q}_f$. The discrepancy is attributed to accumulated approximation errors introduced by (i) kinematic linearization in the boundary-condition transformation, (ii) rescaling applied to acceleration-related parameters, and (iii) subsequent mappings from auxiliary variables to physical angular acceleration (e.g., $(\mathbf{v}, \mathbf{a}) \rightarrow (\boldsymbol{\omega}, \boldsymbol{\alpha})$). These effects become more pronounced for large-angle maneuvers, where linearization errors and propagation sensitivity are amplified. From an operational viewpoint, these observations motivate a feedforward–feedback implementation: the angular-acceleration profile $\boldsymbol{\alpha}(t)$ can serve as a feedforward command, while the $\mathbf{q}(t)$ and $\boldsymbol{\omega}(t)$ profiles can be used as reference trajectories for feedback regulation. Such a structure is expected to reduce the residual terminal mismatch induced by the above approximations.

To assess maneuver-time characteristics, Figure 11b reports the maneuver-time deviation $\Delta T = T_{\text{semi}} - T_{\text{num}}$. The distribution is concentrated around $\Delta T \approx 0$, with an average value of $\overline{\Delta T} = -0.0770$ s, indicating that the maneuver time obtained by the proposed method is generally close to the numerically optimized solution. The clustering of ΔT near zero further suggests that the proposed method can function as a fast pre-screening tool to rapidly gauge the likely existence (and approximate cost) of a feasible solution prior to invoking a computationally heavier numerical solver. Moreover, the semi-closed-form solution can provide a practical warm start when subsequent refinement is required.



(**a**) (**b**)

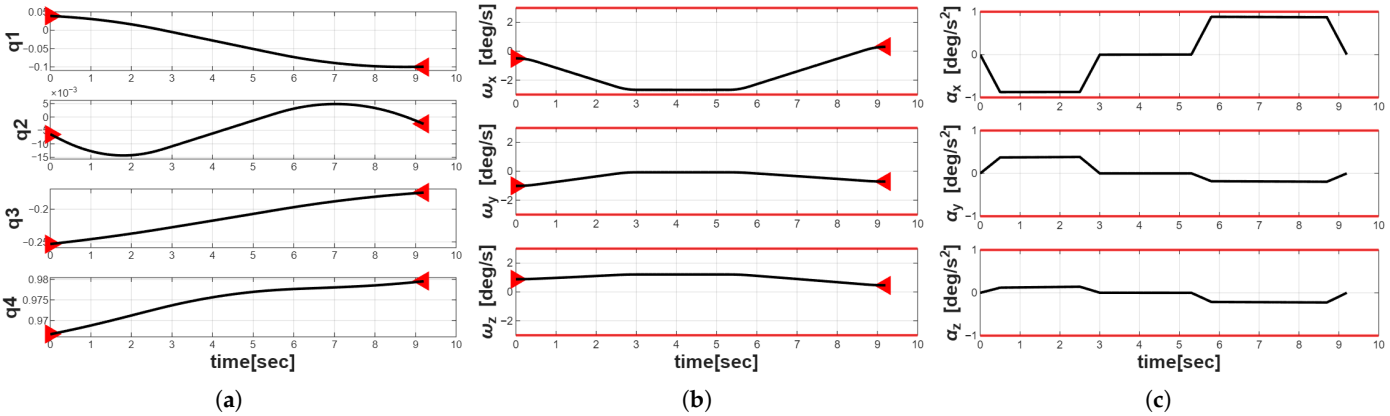
Figure 11. Monte Carlo comparison between the numerical optimization-based method and semi-closed-form solution versus rotation angle: (**a**) attitude error $\theta_{\text{err}} = 2\cos^{-1}(q_{d,4})$; (**b**) maneuver-time deviation $\Delta T = T_{\text{hyb}} - T_{\text{num}}$. The colorbar indicates the number of samples in each bin.

4.3. Feedforward–Feedback Tracking Performance

Section 4.2 showed that the terminal mismatch observed in the semi-closed-form solution can increase with rotation angle due to linearization and mapping approximations. This subsection validates that such residual mismatch can be mitigated in practice by embedding the generated profiles in a feedforward–feedback control structure. Specifically, a deterministic closed-loop simulation is conducted using the variable-limiter cascade-saturation attitude controller proposed in Refs. [18,19]. Since feedback action may introduce additional control effort and thus increase the risk of violating the angular-rate and angular-acceleration constraints, the reference maneuver command is intentionally generated using only 90% of the available bounds. Specifically, the command-generation stage applies tightened limits, $\omega_{\max}^{\text{cmd}} = 0.9\,\omega_{\max}$ and $\alpha_{\max}^{\text{cmd}} = 0.9\,\alpha_{\max}$, so that a residual margin of

approximately 10% of the control authority remains available for feedback regulation. Under this allocation, the proposed method provides the feedforward angular-acceleration profile (nominal command), while the quaternion and angular-rate profiles are used as consistent reference trajectories for tracking. The closed-loop response is then examined to determine whether the remaining margin is sufficient to compensate for the terminal attitude error while respecting the imposed constraints.

Table 5 summarizes the deterministic simulation setup. Under these conditions, the semi-closed-form solution produces the reference profiles shown in Figure 12, yielding a nominal maneuver duration of $t_f = 9.2$ s under the tightened bounds. Figure 13 presents the closed-loop trajectories obtained with the combined feedforward–feedback implementation, including the tracked quaternion and angular-rate responses as well as the applied angular-acceleration profile. Overall, the closed-loop responses closely follow the planned profile shapes while remaining within the imposed bounds (red horizontal lines), indicating that the reserved control authority can be utilized without inducing constraint violations. The red dashed vertical line in Figures 13–15 denotes the nominal terminal time t_f from the profile-generation stage. To quantify how quickly the feedback loop compensates the residual terminal mismatch, the simulation is extended beyond t_f and a settling criterion is adopted: the green dashed vertical line indicates the time instant at which $\theta_{\mathrm{err}}(t) = 0.005^\circ$. In the present case, the time required to satisfy this tolerance after the nominal terminal time is approximately 0.84 s, which provides a practical measure of the additional regulation effort needed to remove the terminal residuals. The feedforward/feedback torque decomposition in Figure 14 further clarifies the control-action allocation. The feedforward torque $\boldsymbol{\tau}_{\mathrm{ff}}(t)$ accounts for the primary maneuvering effort implied by the profile generated by a semi-closed-form solution, whereas the feedback torque $\boldsymbol{\tau}_{\mathrm{fb}}(t)$ becomes more pronounced as the maneuver progresses and particularly near the terminal segment to reject accumulated errors. Consistent with this behavior, the tracking-error histories in Figure 15 show that increased feedback activity is accompanied by a reduction in trajectory errors, culminating in convergence below the prescribed attitude-error tolerance. These results support that the residual terminal mismatch associated with approximations inherent in the semi-closed-form solution can be practically compensated in closed-loop operation using a feedforward–feedback structure while preserving feasibility margins.

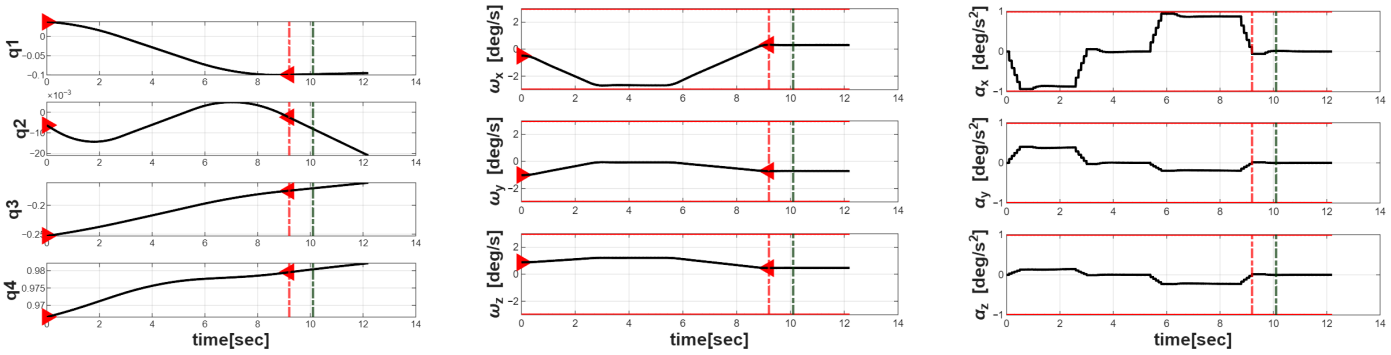


(**a**) (**b**) (**c**)

Figure 12. Reference maneuver profiles used for the feedforward–feedback tracking simulation: (**a**) quaternion trajectory $\mathbf{q}(t)$; (**b**) angular-rate profile $\boldsymbol{\omega}(t)$; (**c**) angular-acceleration profile $\boldsymbol{\alpha}(t)$. The reference command is generated using tightened bounds, $\omega_{\max}^{\mathrm{cmd}} = 0.9\,\omega_{\max}$ and $\alpha_{\max}^{\mathrm{cmd}} = 0.9\,\alpha_{\max}$, so that approximately 10% of the control authority is reserved for feedback regulation. The red horizontal lines indicate the corresponding bounds.

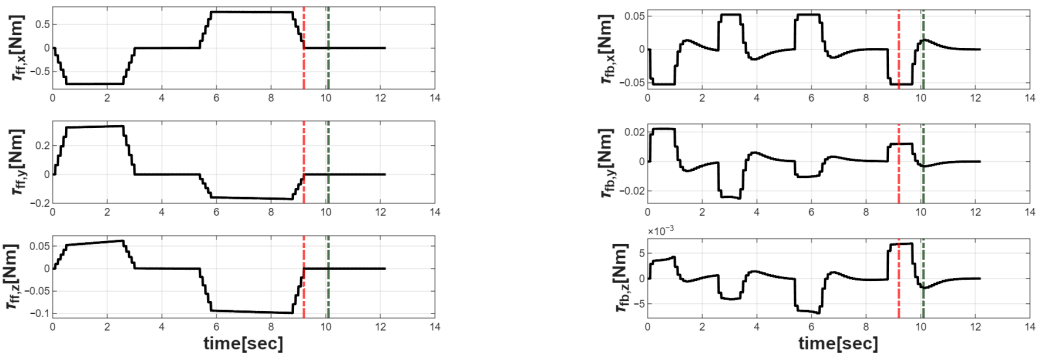
Table 5. Simulation conditions.

Category	Quantity	Value
Boundary conditions	$\boldsymbol{\theta}_0$ [deg]	$[\ 4.129, -1.837, -29.256]^T$
	$\boldsymbol{\omega}_0$ [deg/s]	$[\ -0.489, -1.013, \ 0.883]^T$
	$\boldsymbol{\theta}_f$ [deg]	$[-11.169, -0.605, -18.676]^T$
	$\boldsymbol{\omega}_f$ [deg/s]	$[\ 0.306, -0.711, \ 0.4620]^T$
Constraints/parameters	$\alpha_{\max}$ [deg/s^2]	1
	$\omega_{\max}$ [deg/s]	3
	t_r [s]	0.5
	Δt_{prof} [s] (Profile discretization step)	0.1
Spacecraft	$\mathbf{I}$ [kg·m^2] (Inertia matrix)	diag(50, 50, 25)
Attitude controller	Bandwidth ω_n [rad/s]	3
	Damping ratio ζ [-]	0.9
	Δt_c [s] (Controller sampling period)	0.1



(**a**) (**b**) (**c**)

Figure 13. Closed-loop simulation results with the feedforward–feedback implementation: (**a**) quaternion trajectory $\mathbf{q}(t)$; (**b**) angular-rate trajectory $\boldsymbol{\omega}(t)$; (**c**) angular-acceleration trajectory $\boldsymbol{\alpha}(t)$. The red horizontal lines indicate the corresponding bounds. The red dashed vertical line denotes the nominal terminal time t_f (from the profile-generation stage), and the green dashed vertical line denotes the time at which the attitude-error angle satisfies $\theta_{\text{err}}(t) = 0.005°$. For $t > t_f$, the angular rate is held constant at the terminal value, i.e., $\boldsymbol{\omega}(t) \equiv \boldsymbol{\omega}(t_f)$, and the quaternion in (**a**) is obtained by propagating the quaternion kinematics under this constant-rate assumption.



(**a**) (**b**)

Figure 14. Control torque components used in the feedforward–feedback simulation: (**a**) feedforward torque $\boldsymbol{\tau}_{\text{ff}}(t)$ obtained from the semi-closed-form solution; (**b**) feedback torque $\boldsymbol{\tau}_{\text{fb}}(t)$ produced by the attitude controller to track the reference trajectories and compensate residual errors. The red dashed vertical line denotes the nominal terminal time t_f, and the green dashed vertical line denotes the time at which $\theta_{\text{err}}(t) = 0.005°$.

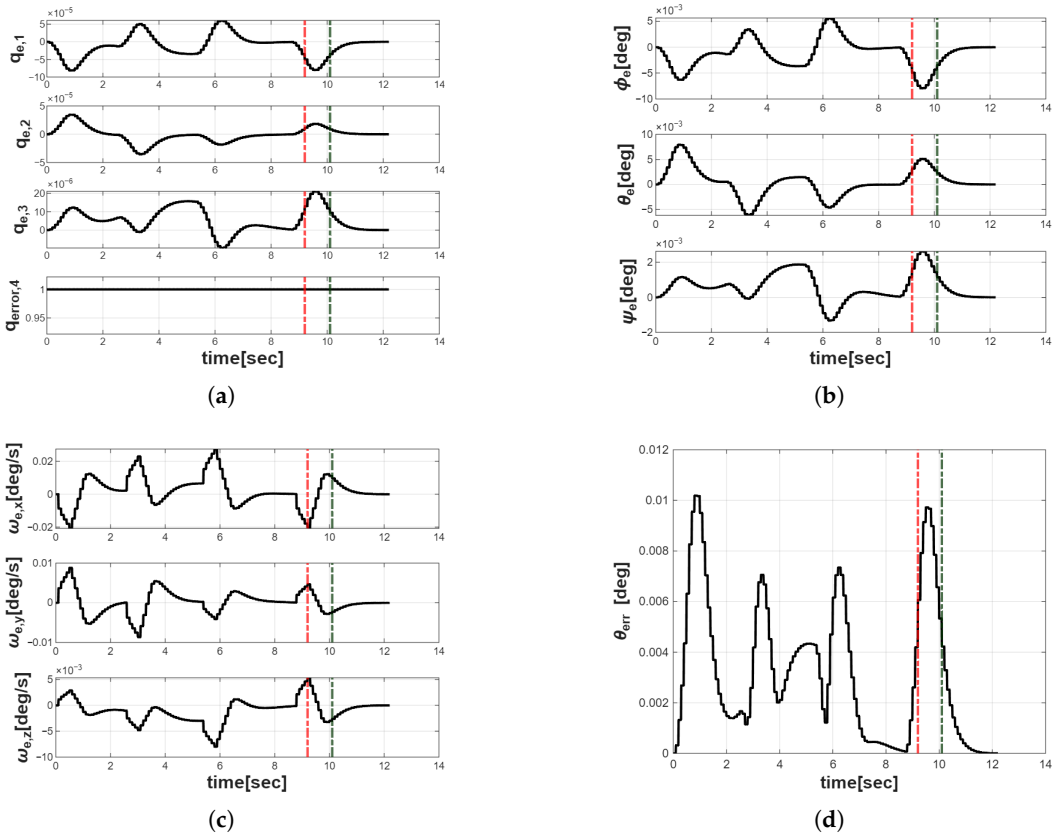


Figure 15. Tracking-error histories obtained from the feedforward–feedback simulation: (**a**) quaternion error $\mathbf{q}_e(t)$; (**b**) Euler-angle error $\boldsymbol{\theta}_e(t)$; (**c**) angular-rate error $\boldsymbol{\omega}_e(t)$; (**d**) attitude-error angle $\theta_{\mathrm{err}}(t)$. The red dashed vertical line denotes the nominal terminal time t_f, and the green dashed vertical line denotes the time at which $\theta_{\mathrm{err}}(t) = 0.005^\circ$ (settling criterion).

5. Conclusions

This paper presented a semi-closed-form profile generator that augments a closed-form solution with an iterative rescale refinement to improve feasibility and optimality under angular-rate and angular-acceleration constraints. Numerical case studies and Monte Carlo evaluations demonstrated that the proposed method can (i) recover feasibility in constraint-violating cases by rescaling maneuver parameters while preserving the prescribed profile structure and satisfying the boundary conditions, and (ii) mitigate conservatism in overly conservative solutions by systematically driving the solution toward the active constraint boundary. Comparisons with a numerical minimum-time solver further indicated that the proposed method yields maneuver times close to those of the numerically optimized solutions. Meanwhile, the terminal attitude mismatch introduced by approximation effects (e.g., kinematic linearization and the mapping from the auxiliary variables to the physical variables) tends to increase with rotation angle; this motivates the use of the proposed method as a fast pre-screening and warm-start mechanism and, when necessary, as a feedforward reference augmented by feedback tracking. Although the computation time increases due to the iterative recalibration, the resulting runtime may remain compatible with on-board use when weighed against the improvements in feasibility recovery and enhanced optimality.

Author Contributions: Conceptualization, S.-H.J. and S.-H.M.; methodology, S.-H.J.; software, S.-H.J. and S.-H.M.; validation, S.-H.J.; formal analysis, S.-H.J.; investigation, S.-H.J.; writing—original draft preparation, S.-H.J.; writing—review and editing, S.-H.J. and S.-H.M.; visualization, S.-H.J.; supervision, S.-H.M. All authors have read and agreed to the published version of the manuscript.

Funding: This work was supported by Inha University research grant.

Data Availability Statement: The original contributions presented in this study are included in the article. Further inquiries can be directed to the corresponding authors.

Conflicts of Interest: The authors declare no conflicts of interest.

References

1. Lee, D.; Song, Y.-J. Single-axis, spin-to-spin slew maneuvers under a finite jerk constraint. *J. Guid. Control Dyn.* **2019**, *42*, 2116–2123. [CrossRef]
2. Thompson, A.B. Minimum jerk attitude slew maneuvers. In Proceedings of the AIAA SciTech Forum, Orlando, FL, USA, 6–10 January 2020.
3. Lee, D.; Song, Y.-J. Closed-Form Solutions for Single-Axis Slew Maneuvers Under a Fixed Final Time Constraint. *Int. J. Aeronaut. Space Sci.* **2024**, *25*, 635–646. [CrossRef]
4. Lee, J.; Lee, D. Closed-Form Solution for the Absolute Effort Minimization Problem for Single-Axis, Spin-to-Spin Slew Maneuvers. *Int. J. Aeronaut. Space Sci.* **2025**, *26*, 2768–2784. [CrossRef]
5. Bai, X.; Junkins, J.L. New results for time-optimal three-axis reorientation of a rigid spacecraft. *J. Guid. Control Dyn.* **2009**, *32*, 1071–1076. [CrossRef]
6. Bilimoria, K.D.; Wie, B. Time-optimal three-axis reorientation of a rigid spacecraft. *J. Guid. Control Dyn.* **1993**, *16*, 446–452.
7. Mok, S.-H.; Bang, H.; Kim, H.-S. Analytical solution for attitude command generation of agile spacecraft. *J. Korean Soc. Aeronaut. Space Sci.* **2018**, *46*, 639–651. (In Korean) [CrossRef]
8. Mok, S.-H.; Bang, H.; Lee, D. Closed-form solution of attitude command generation for spin-to-spin maneuver. *Adv. Space Res.* **2023**, *71*, 676–691. [CrossRef]
9. Fleming, A.; Ross, I.M. Singularity-Free Optimal Steering of Control Moment Gyros. *Adv. Astronaut. Sci.* **2006**, *123*, 2681–2700.
10. Fleming, A.; Ross, I.M. Optimal Control of Spinning Axisymmetric Spacecraft: A Pseudospectral Approach. In Proceedings of the AIAA Guidance, Navigation, and Control Conference, Honolulu, HI, USA, 18–21 August 2008.
11. Fleming, A.; Sekhavat, P.; Ross, I.M. Constrained, Minimum-Time Maneuvers for CMG Actuated Spacecraft. *Adv. Astronaut. Sci.* **2009**, *135*, 1009–1028.
12. Fleming, A.; Sekhavat, P.; Ross, I.M. Minimum-Time Reorientation of a Rigid Body. *J. Guid. Control Dyn.* **2010**, *33*, 160–170.
13. Karpenko, M.; Bhatt, S.; Bedrossian, N.; Ross, I.M. Flight Implementation of Shortest-Time Maneuvers for Imaging Satellites. *J. Guid. Control Dyn.* **2014**, *37*, 1069–1079. [CrossRef]
14. Boyarko, G.; Romano, M.; Yakimenko, O. Time-optimal reorientation of a spacecraft using an inverse dynamics optimization method. *J. Guid. Control Dyn.* **2011**, *34*, 1197–1208. [CrossRef]
15. Ventura, J.; Romano, M.; Walter, U. Performance evaluation of the inverse dynamics method for optimal spacecraft reorientation. *Acta Astronaut.* **2015**, *110*, 266–278. [CrossRef]
16. Wu, C.; Xu, R.; Zhu, S.; Cui, P. Time-optimal spacecraft attitude maneuver path planning under boundary and pointing constraints. *Acta Astronaut.* **2017**, *137*, 128–137. [CrossRef]
17. Lafontaine, J.D.; Peuvedic, C.L. Autonomous generation of guidance profiles for constrained, minimum-time, large-angle attitude maneuvers. In Proceedings of the AAS/AIAA Space Flight Mechanics Meeting, Copper Mountain, CO, USA, 23–27 January 2005.
18. Wie, B.; Lu, J. Feedback control logic for spacecraft eigenaxis rotations under slew rate and control constraints. *J. Guid. Control Dyn.* **1995**, *18*, 1372–1379. [CrossRef]
19. Wie, B.; Bailey, C.; Heiberg, C. Rapid multitarget acquisition and pointing control of agile spacecraft. *J. Guid. Control Dyn.* **2002**, *25*, 96–104. [CrossRef]

Disclaimer/Publisher's Note: The statements, opinions and data contained in all publications are solely those of the individual author(s) and contributor(s) and not of MDPI and/or the editor(s). MDPI and/or the editor(s) disclaim responsibility for any injury to people or property resulting from any ideas, methods, instructions or products referred to in the content.